Designing Ionic Ir(III) Cyclometalated Complexes as Photocatalysts for Light Assisted ATRP of MMA. A Combined Experimental and Mechanistic Study

Designing Ionic Ir(III) Cyclometalated Complexes as Photocatalysts for Light Assisted ATRP of MMA. A Combined Experimental and Mechanistic Study

Giulia Vigarani,[a] Edoardo Marchini,[b]* Eleonora Previati,[a] Loris Giorgini,[a] Stefano Zacchini,[a] Roberto Argazzi,[c] Massimiliano Massi,[d] Valentina Fiorini,[a]* Stefano Caramori,[b] and Stefano Stagni [a]*

[a]: *Department of Industrial Chemistry "Toso Montanari", University of Bologna, Via P. Gobetti 85, 40129 - Bologna, Italy*

[b]: *Department of Chemical, Pharmaceutical and Agricultural Sciences, University of Ferrara, via Luigi Borsari 46, 44121 Ferrara, Italy*

[c]: *CNR-ISOF c/o Department of Chemical, Pharmaceutical and Agricultural Sciences, University of Ferrara, Via L. Borsari 46, 44121, Ferrara, Italy*

[d]: *Department of Chemistry, Curtin University, Bentley, Western Australia 6102, Australia*

Abstract

A new family of ionic Ir(III) cyclometalated complexes with general formula $[Ir(C^N)_2(N^N)][Br]$, was designed and prepared to be assessed as photocalysts for the visible light assisted ATRP polymerization of MMA. To this purpose, our design strategy involved both: i) the decoration of the cyclometalating (C^N) and the ancillary (N^N) ligands with various electron withdrawing and/or electron donor substituents and, ii) the use of Br^- as the counter anion for these cationic Ir(III) species. After an extensive screening in which the $[Ir(C^N)_2(N^N)][Br]$-type compounds were compared to the model neutral complex *fac*-$[Ir(ppy)_3]$, the "fully" amino-substituted ion pairs abbreviated as **[10][Br]** and **[11][Br]**, exhibited the best photocatalytic performances under irradiation with CFL lamps. It is worth noting that the outcomes of transient absorption spectroscopy (TAS) experiments combined with theoretical DFT calculations, allowed to corroborate the role played by the Ir(III) complexes in the mechanism responsible the photoATRP process, and suggested the rationalization of the different performances that were highlighted by our Ir(III) catalyst in the visible light assisted photopolymerization of MMA.

Introduction

As from the late 2000's, the pioneering research works reported by the groups of Macmillan,[1] Yoon,[2] and Stephenson,[3] paved the way for the exploitation of visible light-assisted photoredox catalysis promoted by photoactive transition metal complexes. Beyond to represent a major breakthrough in the area of modern organic synthesis,[4] the concepts underlying the use of Ru(II) and Ir(III) based photoredox catalysts have been transferred to a to variety of visible light assisted polymerization processes, including free radical, cationic and controlled radical polymerizations (CRPs), such as the ones relying on RAFT (reversible addition-fragmentation chain transfer), and ATRP (atom transfer radical polymerization) based techniques. [5], [6] In this latter regard, a notable example of ATRP promoted by an Ir(III)-based photocatalyst was reported in 2012 by Hawker and Fors.[7a] More specifically, the archetype of tris homoleptic Ir(III) cyclometalated complexes, *fac*-[Ir(ppy)$_3$] (ppy = 2-phenylpyridine), was employed as photocatalyst for the photo ATRP of methyl methacrylate (MMA) occurring upon irradiation from a 50 W continuous fluorescent lamp (CFL) and in the presence of ethyl α–bromophenyl acetate (EBPA) as the radical initiator. From a mechanistic point of view, the whole catalytic cycle was supposed to begin with an oxidative electron transfer directed from the photoexcited *fac*-[Ir(ppy)$_3$]* to the radical initiator (EBPA), which in the presence of the MMA monomer starts the polymerization. Then, the so-formed Ir(IV) ionic couple [Ir(ppy)$_3$][Br] complete the catalytic process by the back halogen transfer to the propagating radical, thereby restoring both *fac*-[Ir(ppy)$_3$] as well as the dormant species. In this way, temporal and structural control over the growing polymeric chains was reached upon adjusting the loading of the Ir(III) catalyst at 0.005 mol.%. Accepted this oxidative route, it could be assumed that features such as long lived excited states of triplet manifold (^{3}T), associated with peculiarly low ground state oxidation potential, can be considered as the factors that favoured the use of *fac*-[Ir(ppy)$_3$] as an efficient photoredox catalyst for controlled radical polymerizations.[7a][8] Nevertheless, one of the major drawbacks associated with *fac*-[Ir(ppy)$_3$], and in general, with homoleptic tris-cyclometalated Ir(III) complexes, is related to the often severe and unfavorable conditions required for their synthesis.[9a-c] Instead, heteroleptic Ir(III) based species of the type [Ir(C^N)$_2$(N^N)]$^{+/0/-}$ usually require milder and more convenient preparation procedures,[10] and the introduction of an ancillary ligand (N^N) maximize the opportunity to tailor the catalysts properties to the reaction needs, as the result of the modulation of both excited state properties and redox behaviour. The validity of this approach was first demonstrated in reports from Lalevée and coworkers, [11] where the systematic tuning of both absorption and redox properties led to the obtainment a series of anionic,

cationic and neutrally charged heteroleptic Ir(III) catalysts for free radical, cationic and controlled photopolymerizations. With the aim to extend the scope of the Hawker and Fors protocol[7a] to heteroleptic Ir(III) compounds, we designed and synthesized new ionic Ir(III) complexes with general formula $[Ir(C^N)_2(N^N)][X]$ to be assessed as catalysts for the photo-ATRP of MMA. More specifically, inspired by the rational ligand design strategy adopted by Matyjaszewski and co-workers throughout the entire ATRP development,[12] and keeping in mind the unique properties of cyclometalated Ir(III) complexes, we have decided to tune both ppy-based cyclometalating (C^N) and 2,2' bipyridine-type ancillary (N^N) ligands with the introduction of electron withdrawing (EW) and/or electron donor (ED) functional groups (Scheme 1). In particular, with respect to (N^N), the 2,2' bipyridine (bpy) scaffold was decorated at the 4 and 4' positions with two dimethylamino $(-NMe_2)_2$ or two pyrrolidine $(-pyr)_2$ group to ensure advantageous electronic effects, as in $[Cu^{I}(TPMA^{NMe2})Br]$, which was listed among the most active copper ATRP catalyst so far.[13] In addition, relative to our $[Ir(C^N)_2(N^N)][X]$ -type structures, the role of the counterion $[X^-]$ in the photo ATRP process was investigated for the first time by testing the bromide derivatives $[Ir(C^N)_2(N^N)][Br]$, in comparison to the more frequently occurring hexafluorophosphate $[PF_6^-]$ and tetrafluoroborate $[BF_4^-]$ salts. Importantly, transient absorption spectroscopy (TAS) measurements combined with theoretical DFT calculations were performed to gain insights about the role of the Ir(III) species in our photo-ATRP reaction conditions, thereby suggesting the rationalization of their photo ATRP performances and, hopefully, paving the way for a better understanding of the structure-activity relationship that the newly designed ionic Ir(III)-based complexes should possess for being employed in these visible-assisted controlled radical polymerization processes.

Result and Discussions

Synthesis

The ionic Ir(III) complexes described herein were obtained starting from the preparation of both ancillary (N^N) and cyclometalated (C^N) ligands. With respect to ancillary ligands (N^N), the 2,2' bipyridine scaffold was decorated at the 4 and 4' positions with two N-dimethylamino (bpy-$(NMe_2)_2$) or two N-pyrrolidyl (bpy-$(pyr)_2$) elettron donor groups by adapting the procedure reported by Wenger and coworkers.[14] Cyclometalating (C^N) ligands were prepared according to standard Suzuki-Miyaura coupling protocol involving the reaction between the appropriate bromopyridine and variously substituted phenyl boronic acids.[15] The targeted cationic Ir(III) complexes were then obtained under mild conditions by reaction of the appropriate $[Ir(C^N)\text{-}\mu\text{-}Cl]_2$dimer [16] with a slight

excess of bpy-$(NMe_2)_2$ or bpy-$(pyr)_2$ in a DCM/MeOH 3:1 mixture at room temperature (Figure 1, top). Anion metathesis, followed by a simple column-chromatography work-up gave pure samples of Ir(III) catalysts. All the synthesized ligands and complexes were fully characterized by $^{1}H/^{13}C$ NMR and ESI-MS, which confirmed the predicted molecular structures (See Experimental Section and Supporting Information for further synthetic and spectroscopic details).

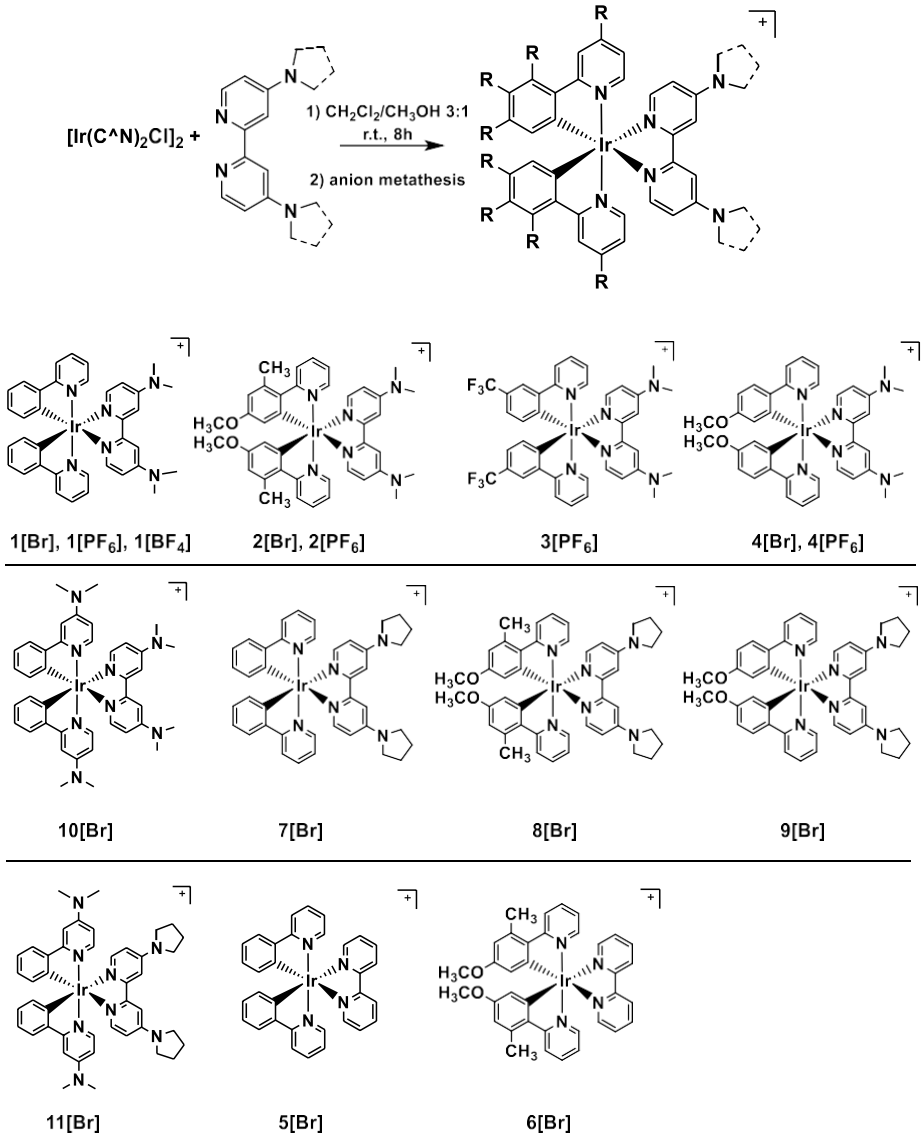

Scheme 1: Synthetic route (top) of all the Ir(III) complexes described in this work (bottom)

X-Ray Crystallography

Further evidences in support of the $^{1}H/^{13}C$ NMR and ESI-MS characterizations came from for X-ray diffraction on single crystals of **[1][BF$_4$]·solv** and **[2][PF$_6$]·CH$_2$Cl$_2$** (Figure 1, Table S4, SI). Several examples of $[Ir(C^N)_2(N^N)]^+$ complexes (C^N = ppy and substituted ppy; N^N = bpy and substituted bpy) have been structurally characterized.[17] Nonetheless, $[Ir(3CHO\text{-}ppy)_2(bpy\text{-}(NMe_2)_2)]^+$ is the only compound of this type containing the bpy-$(NMe_2)_2$ ligand, which has been structurally characterized.[18] Similarly, to the best of our knowledge, $[Ir(2Me\text{-}4OMe\text{-}ppy)_2(acac)]$ is the only complex containing the 2Me-4OMe-ppy ligand whose structure has been reported in the literature.[19] The bonding parameters of **1[BF$_4$]** and **2[PF$_6$]** are comparable to those reported for these complexes. Thus, the Ir(1)-N(1) [2.127(4) and 2.138(4) Å for **1[BF$_4$]** and **2[PF$_6$]**, respectively] and Ir(1)-N(2) [2.128(4) and 2.137(3) Å] distances are sensibly longer than Ir(1)-N(3) [2.043(4) and 2.037(4) Å] and Ir(1)-N(4) [2.030(4) and 2.034(4) Å], due to the trans effect of the metalated C-atoms. Indeed, complexes **1[BF$_4$]** and **2[PF$_6$]** display a distorted octahedral geometry, with the metalated carbons in relative *cis* position and *trans* to the N-atoms of the bpy-$(NMe_2)_2$ ligand. As found in related complexes, the bite angle of the metalated phenyl-pyridine [79.33(16)-80.6(2) °] is larger than that of the bipyridine ligands [75.58(13)-76.02(17) °].[20]

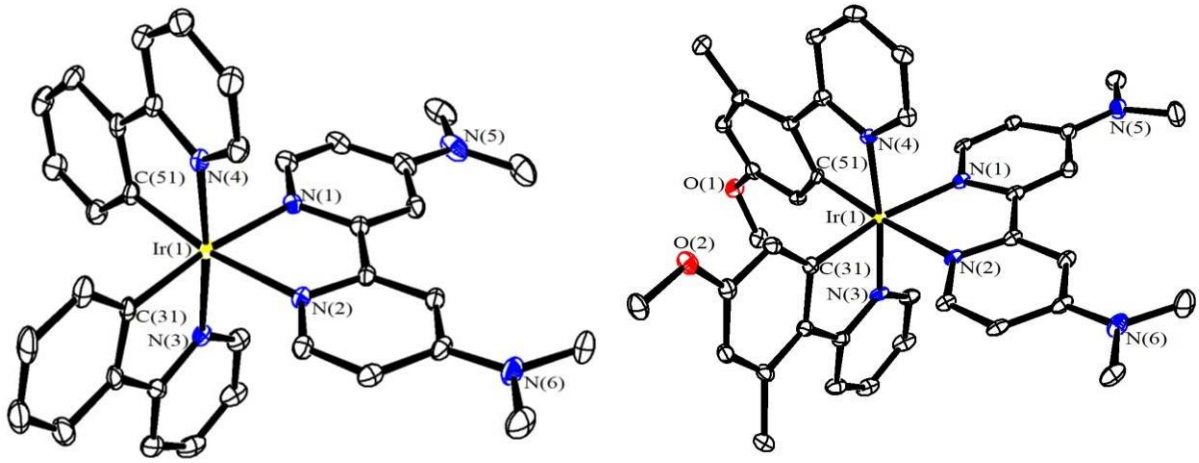

Figure 1: (sx) Molecular structure of **1[BF$_4$]** with key atoms labelled. H-atoms have been omitted for clarity. Displacement ellipsoids are at the 30% probability level. Selected bond lengths (Å) and angles (°): Ir(1)-N(1) 2.127(4), Ir(1)-N(2) 2.128(4), Ir(1)-N(3) 2.043(4), Ir(1)-N(4) 2.030(4), Ir(1)-C(31) 1.999(5), Ir(1)-C(51) 2.012(5), N(1)-Ir(1)-C(31) 172.29(19), N(2)-Ir(1)-C(51) 170.6(2), N(3)-Ir(1)-N(4) 174.31(17), N(1)-Ir(1)-N(2) 76.02(17), C(31)-Ir(1)-N(3) 80.6(2), C(51)-Ir(1)-N(4) 80.2(2), sum at N(5) 359.9(10), sum at N(6) 360.0(10); **(dx)** Molecular structure of **2[PF$_6$]** with key atoms labelled. H-atoms have been omitted for clarity. Displacement ellipsoids are at the 30% probability level. Selected bond lengths (Å) and angles (°): Ir(1)-N(1) 2.138(4), Ir(1)-N(2) 2.137(3), Ir(1)-N(3) 2.037(4), Ir(1)-N(4) 2.034(4), Ir(1)-C(31) 2.005(4), Ir(1)-C(51) 2.007(4), N(1)-Ir(1)-C(31) 169.60(15), N(2)-Ir(1)-C(51) 175.57(15), N(3)-Ir(1)-N(4) 172.64(14), N(1)-Ir(1)-N(2) 75.58(13), C(31)-Ir(1)-N(3) 79.89(17), C(51)-Ir(1)-N(4) 79.33(16), sum at N(5) 359.9(7), sum at N(6) 360.0(7)

Photophysical Properties

Table 1: Photophysical Characterization of Ir(III) catalysts presented in this work

Complex	**Absorption**	**Emission 298 K[a, b]**					**Emission 77 K[c]**	
CH_2Cl_2 as the solvent, 10^{-5}M	λ(nm) 10^{-4}ε ($cm^{-1}M^{-1}$)	λ_{em} (nm)	τ_{ox} (μs)	τ_{deox} (μs)	φ_{ox} (%)	φ_{deox} (%)	λ_{em} (nm)	τ (μs)
1[Br]	268 (2.87), 366 (0.54), 432 (0.23)	488, 518	0.09	1.5	3	14	486, 524	2.1
2[Br]	267 (8.59), 282 (7.60), 370 (1.59)	522	0.10	1.2	4	35	482, 514	2.9
3[PF_6]	267 (7.57), 354 (1.21), 386 (0.85), 420 (0.26)	474, 502	0.18	2.2	5.2	60	472, 508	3.4
4[Br]	268 (8.20), 289 (7.35), 365 (1.47)	514	0.10	1.6	5	35	476, 512	2.7
7[Br]	268 (4.79), 360 (0.88), 430 (0.30)	486, 516	0.08	1.1	2	34	490, 512, 550	2.3
8[Br]	268 (3.08), 287 (2.66), 370 (0.80), 420 (0.37)	516	0.07	1.0	2	25	498	2.8
9[Br]	268(4.61), 293(4.16), 356(1.14), 400 (0.49)	482, 512	0.08	0.7	2	22	478, 514, 552	3.4
10[Br]	270 (5.39), 317 (1.93), 360 (0.94), 427 (0.26)	564	0.08	1.0	2	32	516, 548	5.6
11[Br]	271 (5.47), 316 (1.98), 360 (0.96), 424 (0.25)	556	0.07	1.0	3	36	528	4.5
5[Br]	256 (9.30), 268 (9.17), 380 (1.05), 410 (0.54)	598	0.19	0.5	8	16	514, 548	3.5
6[Br]	279 (8.08), 309 (4.05), 332 (2.65), 380 (0.76)	610	0.15	0.3	10	25	522, 550	3.9
***fac*-[Ir(ppy)$_3$]**	243 (3.30), 283 (3.23), 381 (0.65)	522 520[d]f	0.05 0.087[d]	0.7 1.2[d]	1.9	25.6	512, 548	4.4

[a]: "ox" = air equilibrated solutions, "deox" = deoxygenated solutions under argon atmosphere; [b]: vs $[Ru(bpy)_3]Cl_2/H_2O$ ($\Phi_r = 0.028$)[21]; [c]: in frozen CH_2Cl_2; [d] in DMF.

Even if different counterions were tested to assess their influence on the photoactivated ATRP mechanism, the following discussion is centred only on the bromine **[Br]**$^-$ salts, since both the corresponding hexafluorophosphate **[PF_6]**$^-$ and tetrafluoroborate **[BF_4]**$^-$ saline compounds displayed nearly identical photophysical properties to those observed for the bromine-based complexes (Table S2, Figures S67, S68, S71, S74, S77, SI). The absorption spectra of the Ir(III) species were obtained from diluted (10^{-5}M) CH_2Cl_2 solutions at 298 K. In all cases, intense LC (Ligand Centred) transitions in the UV region, followed by weaker MLCT (Metal to Ligand Charge Transfer) processes tailing in the visible region (Figure 2), were observed. Upon excitation of the corresponding dilute solutions in the MLCT region (λ = 370 nm), all the Ir(III) complexes displayed bright luminescence. In all cases, the triplet character of the excited states was confirmed by the sensitivity to the presence of dissolved O_2 displayed both by quantum yield (Φ) and lifetime (τ) values (Table 1). Vibronically structured profiles were observed for complexes **1[Br]** and **3[PF_6]**, while broad and structureless ones were observed for **2[Br]** and **4[Br]** (Table 1, Figures S69, S77, S72, S75). The

analyses of the emission spectra recorded from the solutions frozen at 77K evidenced the expected *hypsochromic* shift of the emission maxima, together with the appearance of structured profiles, highlighting a behaviour that might account for the interplay of ^{3}LC/^{3}MLCT type emissive excited states.[22]

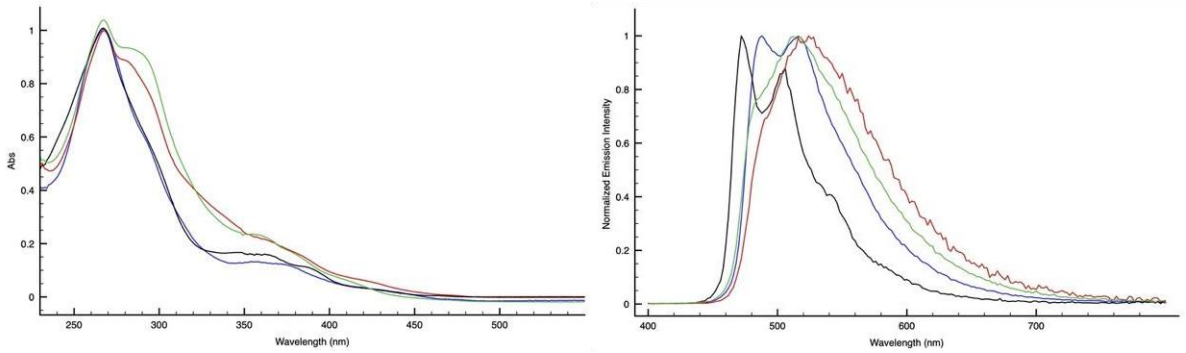

Figure 2: Normalized Absorption (sx) and emission (dx) profiles of Ir(III) catalysts (**1[Br]** blue line, **2[Br]** red line, **3[Br]** black line, **4[Br]** green line)

If compared to the emission profiles displayed by complexes **5[Br]** and **6[Br]** – which are centred at λ_{max}= 598 and 610 nm, respectively) - the introduction of two dimethyl amino (-NMe_2) groups at the 4 and 4' positions of the 2, 2' bpy (N^N) ligand, as in species **1[Br]**-**4[Br]**, led to the shift to higher energies the emission spectra (Figure 2, 3). The influence played by the different substituents on the cyclometalating (C^N) ligand set can be outlined choosing **1[Br]** as reference compound, which showed a vibronically structured emission peaking at λ_{max}= 486, 516 nm. The introduction of electron donor (ED)-substituents in the backbone of the phenylpyridine (ppy) backbone, such as in **2[Br]** and **4[Br]**, resulted in the slight red shifted of the emission profiles and in the enhancement of the quantum yield (Φ) values (Table 1, Figure 4). Instead, the introduction of electron withdrawing (EW) groups, as in **3[PF_6]** (Table 1, Figure 2), produced a blue shift of the structured emission profile together with a consistent enhancement of both lifetimes (τ) and quantum yield values (Φ).

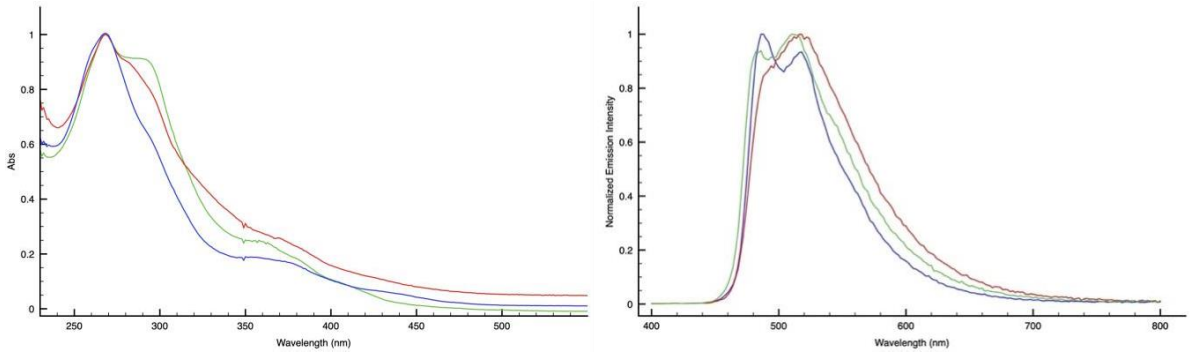

Figure 3: Normalized Absorption (sx) and emission (dx) profiles of Ir(III) catalysts (**7[Br]** blue line, **8[Br]** red line, **9[Br]** green line)

The use of pyrrolidine as ED in the N^N ligand as for **7[Br]**, **8[Br]** and **9[Br]** (Table 1, Figure 3) did not substantially alter the photophysical behavior observed. Indeed, the resulting emission profiles are almost superimposable to those recorded from complexes **1[Br]**-**4[Br]**. Minor differences were only observed for the quantum yield values obtained from deoxygenated solutions (Φ_{deox}), highlighting a trend that might be explained in consideration of the increased rigidity that is brought by the more sterically demanding pyrrolidine ring. Appreciable variations were observed upon the decoration at the N-4 position of the pyridyl ring of the (C^N) ligands with one dimethylamino (NMe_2) group, as in **10[Br]** and **11[Br]**). More specifically, this modification led to a consistent *red-shift* of the emission profile (λ_{max} = 564 nm for **10[Br]** and λ_{max} = 556 nm for **11[Br]**, Figure 4). On the other hand, lifetime (τ) and quantum yield (Φ) values were consistent with those recorded from the other Ir(III) compounds presented herein.

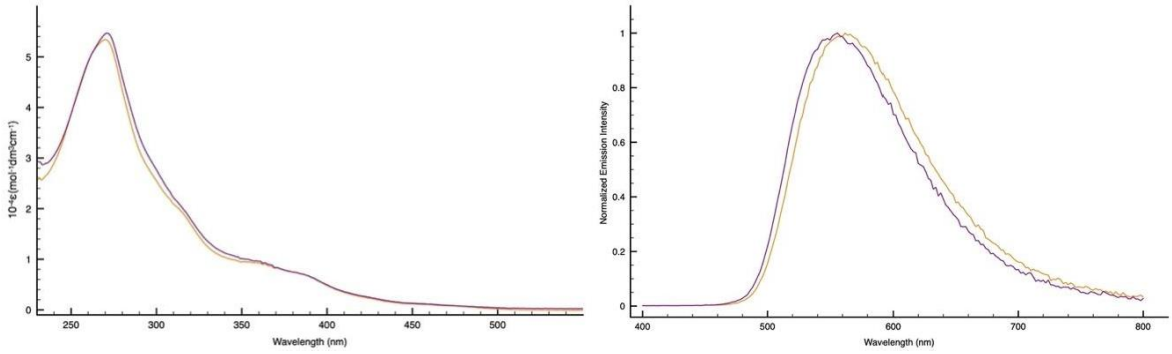

Figure 4: Absorption (sx) and Normalized emission (dx) profiles of Ir(III) catalysts (**10[Br]** orange line, **11[Br]** purple line

Stern Volmer Quenching Studies

Since the catalytic cycle involved in the photo-ATRP reaction is thought to begin with the reduction of an alkyl bromide by an Ir(III)* species,[7a-b] Stern Volmer analysis was performed to clarify if our Ir(III) species together with EBPA, the radical initiator, were suitable for the targeted reaction (Figure 5).

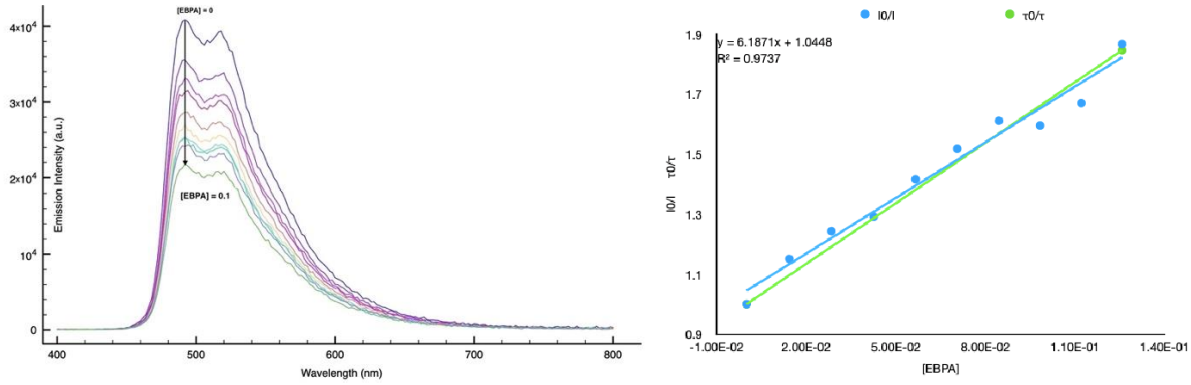

Figure 5: Stern Volmer analyses of **1[Br]** (M = $1.22*10^{-4}$ in DMF) vs EBPA (9x5µL), 298K

In all cases (Table S3, Figures S70, S73, S76, S79, S81, S83, S85, S87), upon increasing concentration of EBPA (from 0 to 0.1 M), a reduction of the Ir(III) -based emission (10^{-4} M solutions in degassed DMF) and of the excited state decays was observed, suggesting that a dynamic quenching mechanism is taking place between our Ir(III) complexes and EBPA.

Redox properties

The redox properties of the compounds described herein were investigated by performing cyclic voltammetry experiments and the relevant data are listed in Table 2.

Table 2: Half-Wave redox potentials for all the reported Ir(III) species (10^{-3}M in anhydrous DMF, $TBAPF_6$ 0.1 M as the supporting electrolyte); SCE and Pt(II) as reference and working electrode, respectively. Scan rate 0.1 V/s; Excited States Redox Potentials; HOMO-LUMO energies

Complex	oxidation vs SCE	reduction vs SCE	E_{ox}^{*a} Ir(III)*/Ir(IV)	E_{red}^{*a} Ir(II)/Ir(III)*	E_{00}^{b}	HOMO[c]	LUMO[c]	GAP
	E(V)	E ½ (V)	(eV)	(eV)	(eV)	(eV)	(eV)	
1[Br]	+1.22	-1.72	-1.32	+0.82	2.54	-5.62	-2.68	2.94
2[Br]	+1.18	-1.72	-1.20	+0.66	2.38	-5.58	-2.68	2.90
3[PF_6]	+1.64	-1.67	-0.98	+0.95	2.62	-6.04	-2.73	3.32
4[Br]	+1.21	-1.72	-1.20	+0.69	2.41	-5.61	-2.68	2.93
5[Br]	+1.30	-1.32	-0.78	+0.77	2.08	-5.70	-3.08	2.62
6[Br]	+1.36	-1.31	-0.67	+0.71	2.03	-5.76	-3.09	2.67
7[Br]	+1.24	-1.74	-1.32	+0.82	2.56	-5.64	-2.66	2.98
8[Br]	+1.14	-1.76	-1.42	+0.75	2.51	-5.54	-2.64	2.90
9[Br]	+1.19	-1.78	-1.37	+0.78	2.56	-5.59	-2.62	2.97
10[Br]	+0.79, +0.97, +1.14	-1.76	-1.41	+0.44	2.20	-5.19	-2.64	2.73
11[Br]	+0.93, +1.16	-1.80	-1.30	+0.43	2.23	-5.33	-2.60	2.73
(bpy-(NMe_2)	+1.20	-0.65^{irr}, -1.08^{irr}, -1.26^{irr}	/	/	/	/	/	/
(ppy-NMe_2)	+1.28	-0.66	/	/	/	/	/	/
***fac*-[Ir(ppy)$_3$] - 12**	+0.70	-2.20	-1.73	+0.23	2.43	-5.10	-2.20	2.90
Fc/Fc^+	+0.51	/	/	/	/	/	/	/

[a]: calculated with $E_{ox}^* = E_{ox}-E_{00}$; $E_{red}^* = E_{red}+E_{00}$[23] [b]: calculated with $E_{HOMO} = -(E_{ox}+4.4eV)$; $E_{LUMO} = -(E_{red}+4.4\ eV)$[24]

In the region of the positive potentials, all the Ir(III) complexes displayed one single process, which is commonly ascribed to the formal oxidation of Ir(III) to Ir(IV). In particular, complex **1[Br]** displayed one process centred at +1.22 V vs SCE (Table 2, Table S1, Figure S55), in accordance with previously reported data.[25] Concerning reductions, the single and reversible process centred at *ca.* -1.72 V

wasassigned to the reduction of the dimethylamino moieties on the (bpy-$(NMe_2)_2$) scaffold.[25] The decoration of cyclometalating (C^N) ligands with ED groups as in **2[Br]** and **4[Br]** did not substantial vary the outcomes, with reversible oxidations at +1.18 V and +1.21 V respectively, and a single cathodic process at -1.72V (Table 2, Table S1, Figures S56, S57). As expected, the ($-CF_3$) group as in **3[PF_6]** (Table 2, Table S1, Figure S58) made the oxidation more difficult (up to +1.64 V) and anticipated the (bpy-$(NMe_2)_2$) reduction of approximately 50 mV (-1.67 V). For (bpy-$(pyr)_2$) -based complexes, similar oxidation values were observed (Table 2, Table S1), but the reductions of pyrrolidine appeared to be slightly harder than the dimethylamino groups (Figures S59, S60, S61). Concerning **10[Br]** and **11[Br]**, the decoration of ppy ligands with a *N-para* dimethylamino group made the anodic region more difficult to interpret, with the occurrence of closely spaced processes. Compound **10[Br]** displayed three oxidation processes at +0.79 V, +0.97 V and +1.14 V (Table 2, Table S1, Figure S63). A single reversible reduction was observed at -1.76 V. In an analogous manner, **11[Br]** displayed two oxidations at +0.93 V and +1.16 V, while a single and reversible reduction was observed at -1.80 V (Table 2, Table S1, Figure S64). This behavior can be traced back to the presence of four different ED groups on both ppy and bpy-based ligands (*i.e.* dimethylamino and/or pyrrolidine), which may undergo oxidation right after the metal center.[25],[26] The ground state redox properties of the proposed Ir(III) catalysts are quite different along the series. The greater the electro-donating ability of the ED groups used, the greater is the extent of HOMO destabilization, lowering thus the oxidation values of these Ir(III) complexes (Table 2). Moreover, both (bpy-$(NMe_2)_2$) and (bpy-$(pyr)_2$) raises the energy of the corresponding LUMOs more evidently compared to unsubstituted bpy (**5[Br]** and **6[Br]**), making harder the corresponding reductions (Table 2, Table S1, Figure S65, S66). The combination of the electrochemical data with the triplet excited state energy (E^{00}, Table 2) leads to the calculation of E_{ox}* and E_{red}*, the excited-state redox potentials. With the exception of **3[PF_6]** and the model compounds **5[Br]** and **6[Br]**, the calculated values suggest how these Ir(III) complexes are good excited-states reductants, making possibly faster the photoinduced electron-transfer to the radical initiator EBPA.

TDDFT calculations

The TDDFT calculation were performed on optimized structures of catalyst **1[Br]**, **10[Br]**, **5[Br]** and of ***fac*-[Ir(ppy)]$_3$** for comparison. Geometry optimization was carried out at the B3LYP/LANL2DZ level, while the TDDFT calculation were run on optimized structures in CH_3CN by using the B3LYP/CEP-121G (relativistic compact effective potential) functional to compute the lowest 40

vertical singlet transitions spanning most of the UV-Vis region.[27] The HOMO energy obtained from these calculations well reproduces the experimental trend in the oxidation potential in the series of Ir(III) complexes investigated (Figure 6, Table S5, Figure S133- S135). The experimental oxidation potentials vary from 0.76 V vs SCE for **10[Br]** to 1.30 V vs SCE for **5[Br]**. If a nearly constant offset of 0.4 eV with respect to the experimental measurements is considered, the same behavior was observed for the computed HOMO. The TD-DFT/B3LYP/CEP-121G calculations well reproduce the experimental absorption envelope of all complexes, showing groups of vertical transitions which span the 3-5 eV interval.

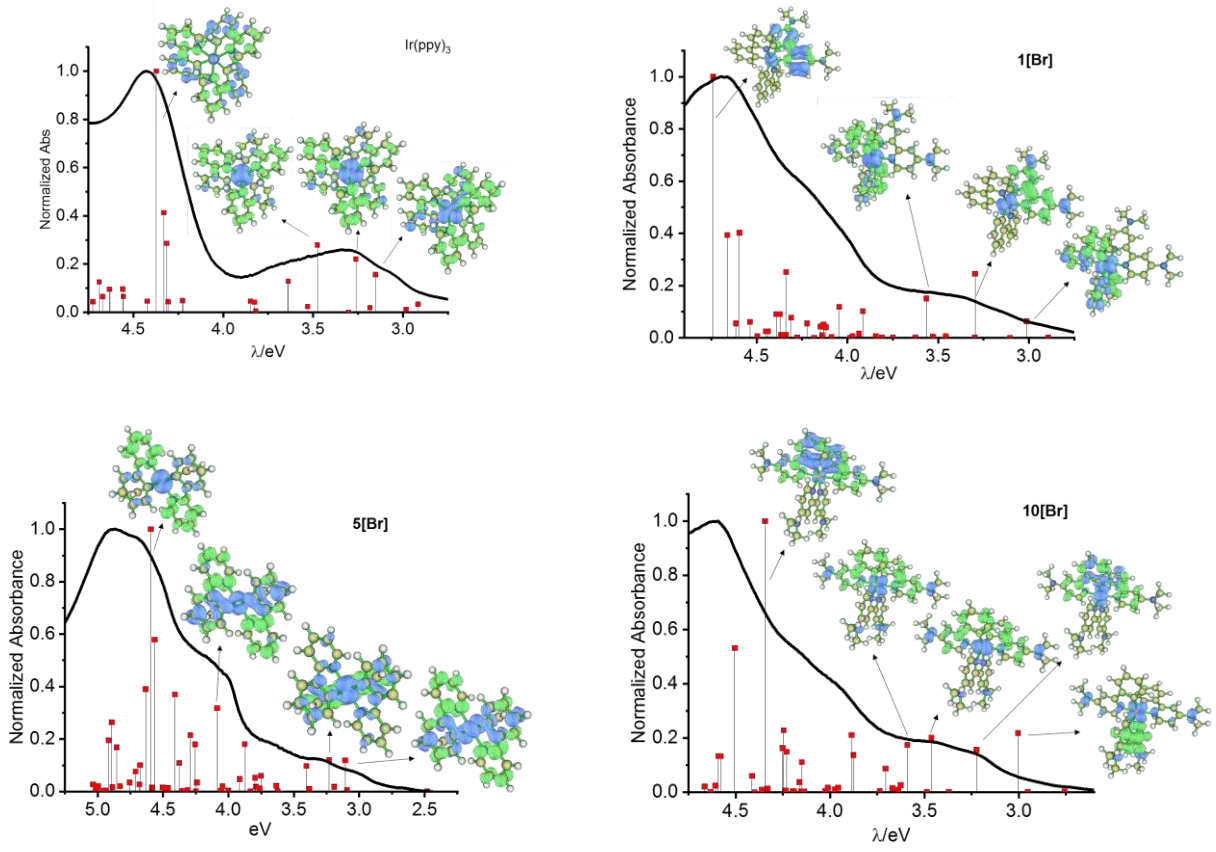

Figure 6: Experimental vs. TD-DFT/B3LYP/LANL2DZ computed vertical excitations (vertical lines surmounted by a red square) in complexes **Ir(ppy)$_3$**, **1[Br]**, **5[Br]** and **10 [Br]** and their relative EDDM maps**.** Experimental spectra have been normalized to the highest absorption band while the vertical transitions were normalized to the most intense one

In most cases a group of two transitions can be identified, with the most intense ones clustered around 4.5 eV. A weaker absorption band, resulting from the overlap of several excitations with a relatively small oscillator strength extends into the near UV and Vis region, up to 2.5 eV in the case of **[5]Br**. On the KS basis, the main contributions to the optical transitions involve mixed excitations from the HOMO, HOMO-1 and HOMO-2 to LUMO, LUMO+1 and LUMO+2 and, in the case of **1[Br]**

and **5[Br]** excitations from HOMO-3 to LUMO+3 are also present (Figure S135). The isodensity maps of the occupied orbitals bear contributions from both the Ir(III) orbitals and those of the ligands. In the case of the homoleptic reference compound *fac*-[**Ir(ppy)$_3$]**, the frontier orbitals are apparently mostly equally delocalized between the metal and the three identical ligands (Figure S135 a), while the heteroleptic complexes **1**, **5** and **10 [Br]** display occupied orbitals bearing main contributions from both metal and phenylpyridine ligands. On the other hand, the lowest unoccupied orbitals have mostly a bipyridine π* character.

The compositional analysis of the HOMO is useful to understand the mixing extent of metal and ligand orbitals in the ground state and also to visualize the spatial distribution of the "hole" created upon oxidation of Ir(III) to Ir(IV). The metal contribution to the HOMO varies in the order *fac*-**[Ir(ppy)$_3$]** (53.06%) > **10[Br]** (43.96%) > **1[Br]** (41.74%) > **5 [Br]** (39.04%), outlining a lower degree of delocalization in *fac*-**[Ir(ppy)$_3$]** and the prevailing MLCT character of its optical transitions. Instead, the optical excitations display a stronger MLCT-ILCT (Intraligand Charge Transfer) nature in the heteroleptic **1-10 [Br]** compounds, which more strongly mix their metal orbitals with the σ and π system of the cyclometalated ligands. The Electron Density Difference Maps (EDDM) (Figures S136-140) are used to generate a "single particle" pictorial view of the change in electron density in these Ir(III) complexes upon light absorption. In particular, the lowest energy EDDM allows to visualize the "electron" and "hole" density distribution at the first singlet excited state (S_1) which is relevant for triggering the photochemical reactions of our interest. Similarly, the S1 electron/hole distribution is expected at the lowest triplet state (T_1) as well. EDDM clearly reveal that the hole density is mainly localized on the iridium core in the case of *fac*-**[Ir(ppy)$_3$]**, corroborating the MLCT assignment to the lowest energy optical excitations. In the **1-10[Br]** series, the hole distribution consistently confirms the stronger mixing with the orbitals of the phenyl-pyridine ligands found with the compositional analysis of the frontier orbitals. Among this series, the hole distribution of **10[Br]** shows a prevailing localization on the iridium center. Upon excitation, the electrons of the Ir(III) complexes are well localized on the π* orbitals of the ligands. As they are located at the periphery of the molecular structure, they can couple favorably with electron acceptors diffusing in solution, giving rise to the oxidative quenching of the excited state. For analogous reasons, the electronic coupling between the hole localized and contracted on the Ir(III) center and an electron donor present in solution is expected to be small, thus retarding charge recombination and partly favoring the appearance of a long lived charge separated state. As far we have observed, the persistence of the charge separated state is not correlated with the degree of hole density on the Ir(III) core, but rather the process

seems to be critically dependent on the electron donor capabilities of the excited state, for which a favorable electronic coupling, arising from the LUMO distribution, must be accompanied by a sufficiently negative excited state potential.

Photo-ATRP of MMA

Table 3: Reaction conditions, molecular weight and polydispersity values for the light mediated ATRP of MMA using the various Ir(III) catalyst described herein. MMA = 0.4 mL, DMF = 1.4 mL

Entry	Cat.	Cat. (mol%)	EBPA (mol%)	M_n theo. (g/mol, 8h)	M_n exp. (g/mol, 8h)	PDI 8h (mean)	χ 8h (%)	Light source
1	**1 [PF_6]**	0.01	0.4	10400	13000	1.6 (1.5)	40.5	LED
2	**1 [BF_4]**	0.01	0.4	10600	9000	1.7 (1.6)	41.5	LED
3	**1 [Br]**	0.01	0.4	11000	8600	1.9 (1.7)	43.1	LED
4	**1 [Br]**	0.01	0.4	11800	10600	1.9 (1.9)	46.2	CFL
5	**1 [Br]**	0.0125	0.4	10500	8500	2.0 (1.9)	41.2	CFL
6	**1 [PF_6]**	0.015	0.4	8600	11300	1.5 (1.4)	33.6	LED
7	**1 [Br]**	0.015	0.4	10400	9200	1.7 (1.7)	40.8	LED
8	**1 [Br]**	0.015	0.4	8500	8100	1.8 (1.9)	32.9	CFL
9	**1 [Br]**	0.02	0.4	8200	6000	1.7 (1.7)	31.7	CFL
10	**2 [PF_6]**	0.01	0.4	10600	6300	1.6 (1.6)	41.5	LED
11	**2 [Br]**	0.01	0.4	8200	6300	1.8 (1.6)	31.7	LED
12	**2 [Br]**	0.01	0.4	9100	7700	2.0 (1.9)	35.3	CFL
13	**2 [Br]**	0.0125	0.4	9800	9100	2.0 (1.9)	38.1	CFL
14	**2 [Br]**	0.015	0.4	7600	7200	1.7 (1.6)	29.6	LED
15	**2 [Br]**	0.02	0.4	8400	7700	1.6 (1.6)	32.7	LED
16	**3 [PF_6]**	0.01	0.4	11300	12900	1.9 (1.6)	44.2	LED
17	**4 [PF_6]**	0.01	0.4	11700	10300	1.7 (1.6)	45.8	LED
18	**4 [Br]**	0.01	0.4	7300	7600	1.7 (1.6)	28.2	LED
19	**4 [Br]**	0.01	0.4	9000	7900	1.7 (1.6)	34.9	CFL
20	**4 [Br]**	0.015	0.4	9900	8800	1.7 (1.8)	38.7	CFL
21	**4 [Br]**	0.02	0.4	11000	9000	1.7 (1.7)	43.2	CFL
22	**7 [Br]**	0.015	0.4	9000	6800	1.8 (1.7)	35.1	CFL
23	**7 [Br]**	0.02	0.4	6600	7500	1.5 (1.5)	25.6	CFL
24	**8 [Br]**	0.015	0.4	9600	8400	1.7 (1.7)	37.6	CFL
25	**8 [Br]**	0.02	0.4	10600	6400	1.6 (1.5)	41.4	CFL
26	**9 [Br]**	0.015	0.4	4200	4100	1.8 (1.6)	15.7	CFL
27	**9 [Br]**	0.02	0.4	5900	6400	1.5 (1.6)	22.5	CFL
28	**10 [Br]**	0.01	0.4	7600	7300	1.7 (1.8)	29.6	CFL
29	**10 [Br]**	0.0125	0.4	11200	7700	1.7 (1.7)	43.7	CFL
30	**10 [Br]**	0.015	0.4	11900	9500	1.6 (1.6)	46.6	CFL
31	**10 [Br]**	0.02	0.4	12000	9800	1.6 (1.6)	47.2	CFL
32	**10 [Br]**	0.02	0.4	3900	17100	1.3 (1.4)	14.8	LED
33	**11 [Br]**	0.01	0.4	5100	5800	1.4 (1.5)	19.4	CFL
34	**11 [Br]**	0.015	0.4	8200	7900	1.4 (1.4)	31.8	CFL
35	**11 [Br]**	0.02	0.4	6600	7100	1.4 (1.4)	25.6	CFL
36	**11 [Br]**	0.02	0.4	2000	4400	1.4 (1.3)	7.1	LED
37	**5 [Br]**	0.01	0.4	-	-	-	0	CFL
38	**5 [Br]**	0.02	0.4	1700	-	-	5.7	LED
39	**6 [Br]**	0.01	0.4	-	-	-	0	LED
40	**6 [Br]**	0.01	0.4	1200	-	-	3.8	CFL
41	**$Ir(ppy)_3$**	0.01	0.4	13200	11300	1.6 (1.5)	51.9	CFL

Following their full characterization, the ionic Ir(III) complexes were tested in the photoactivated ATRP of methyl methacrylate (MMA), which was carried out under argon atmosphere upon exposure to different light sources, such as a white LED strip or two readily available CFL household lamps (see Supporting information, Figures S91-92). A fan was placed above the photoreactor to ensure temperature control over the whole reaction period. Then, in keeping with the protocol

10.1002/chem.202400393

described by Hawker and Fors,[7a] anhydrous and thoroughly degassed DMF was used as the solvent, and the highly reactive ethyl α-bromophenylacetate (hereafter, EBPA) was selected as the radical initiator of our photoinitiated system (Scheme 2).

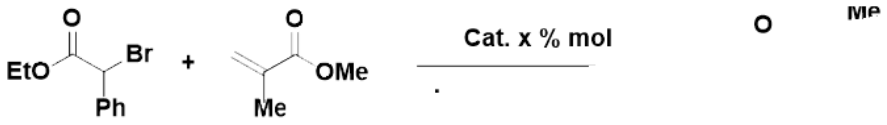

Scheme 2. Photoinduced ATRP of MMA in presence of Ir(III) catalyst and EBPA as initiator

However, a variety of reaction and structural parameters such as light source, the type of cationic Ir(III) catalyst and the nature of the corresponding counterion, were screened to evaluate their impact on the photo ATRP of MMA and, therefore, to accomplish the better optimized conditions for the whole process. Concerning the light source, after 8 hours of exposure at room temperature, both LED and fluorescent lamps photoreactors set-up gave polymers displaying molecular weights (M_n) oscillating between 4 and 11 Kg/mol, with polydispersity index (PDI) ranging from 1.4 to 2.0 and conversion (χ) values spanning from 15 to 47 % (see table 3 and Supporting information, Figures S93-S128). Importantly, if compared to the white LED strip, the irradiation from CFL lamps generally led to better reaction control, with slightly higher conversion values and polymerization profiles consistent with the expected theoretical molecular weight (M_n) values (table 3 and Supporting information, Figures S93-S128). This is probably due to the better overlap between the absorption spectra of Ir(III) complexes and the emission spectra of CFL lamps (see also Supporting information, Figures S93- 128). Another substantial improvement in reaction control was achieved upon the use of the Ir(III) based catalysts under the form of the corresponding bromide salts, *i.e.* the species with general formula $[Ir(C^N)_2(N^N)][Br]$, (Figure 7, entry 1 and entry 3 in Table 3). We rationalized this evidence by considering that in such Ir(III) assisted photo-ATRP protocol, the sole presence of $[Br]^-$ anions, originating both from the radical initiator EBPA and the Ir(III) catalyst, may be one of the key factors for establishing a proper balance between the active and the dormant species.

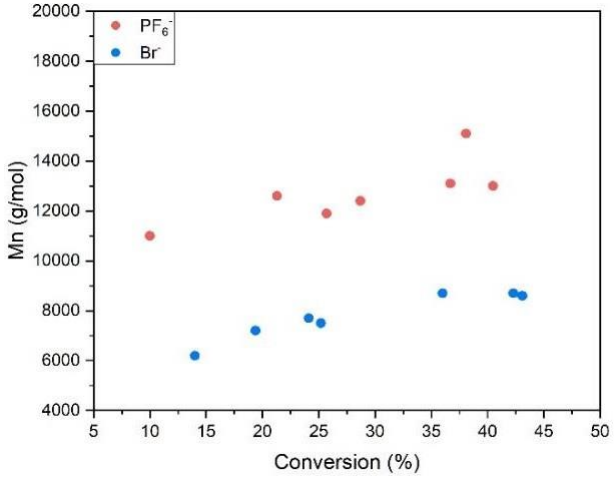

Figure 7: Comparison between **1[PF$_6$]** and **1[Br]** as catalysts in the photo-ATRP of MMA. [MMA]:[EBPA]:[Ir] = 1:0.004:0.01%

In agreement with the proposed mechanism,[7a-b] and with our design strategy, better performances were observed when easily oxidizable Ir(III) complexes were used as catalysts (*i.e.* good excited states reductants). As previously observed for copper-mediated ATRP,[13] we noticed how the introduction of sp^3 hybridized N-moieties on both C^N and/or N^N ligands conferred the desired ground and excited states features to our compounds. (entry 28-36 in table 3). To further support, the use of **5[Br]** and **6[Br]** (without amino groups, entry 37-40 in table 3) did not provide satisfying conversion values and/or control on the polymer growth. In general, the relationship between $\ln(M_0/M)$ vs reaction_time as well as the trend of M_n vs χ were found to be linear within 4 hours (Figure 8), then a slight decrease in slope was observed. The best performances were obtained when **10[Br]** and **11[Br]** were used as catalyst, the best excited states reductants of the series. Good control over the polymerization was reached by employing from 0.01 to 0.02 mol% of both **10[Br]** and **11[Br]**, with molecular weight distribution ranging from 1.7 to 1.4 (**10[Br]**:entries 28-31 in table 3 and Supporting information, Figures S120-124; **11[Br]:** entries 33-35 in table 3 and Supporting information, Figures S125-128) and conversion values spanning from 19 to 47% under CFL irradiation.

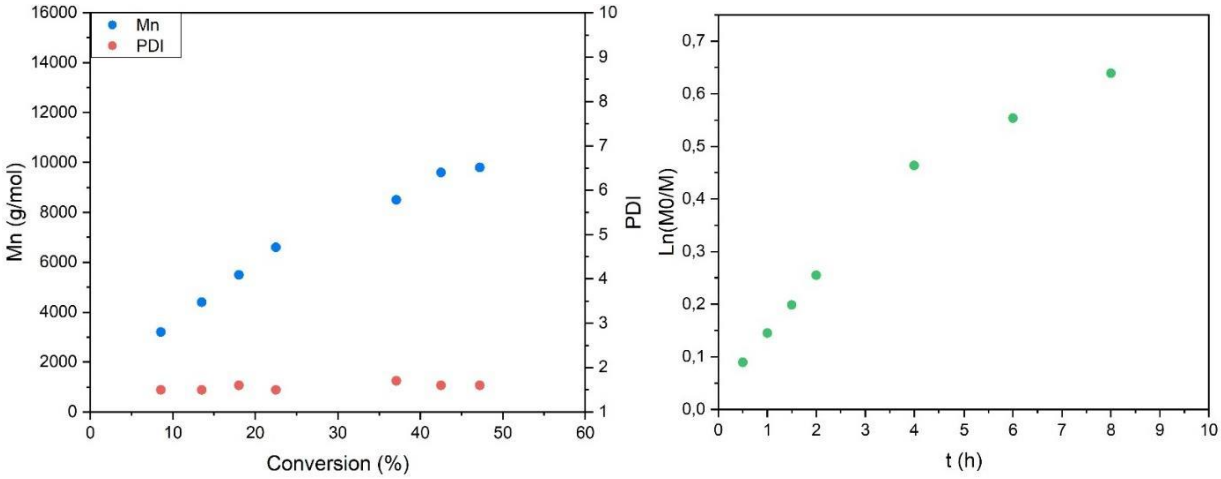

Figure 8: (sx) Polymerization profile of MMA, under argon, CFL set-up; (dx) Kinetic plot; Cat.: **[10]Br**. [MMA]:[EBPA]:[Cat] = 1:0.004:0.02%

Temporal control over the ATRP reaction was demonstrated by switching between dark and light periods, with the lack of any reaction in the absence of irradiation. Indeed, no polymerization was observed when monomer, radical initiator and catalyst were combined for 1 hour in the absence of light. The reaction was then exposed to light for two hours, resulting in almost 15% MMA conversion (Figure 8). The living nature of this photoinitiated system, along with the presence of active bromo groups at the end of the growing polymeric chains, was further demonstrated by using purified PMMA obtained after 4 hours of irradiation as macroinitiator in the polymerization of HMA (hexylmethacrylate) (Scheme 3).

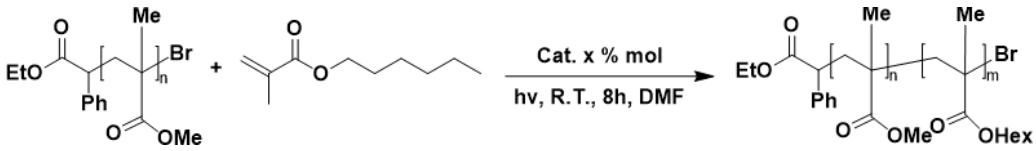

Scheme 3. Synthesis of block copolymer (PMMA-b-PHMA) using PMMA as macroinitiator

The reaction of PMMA-macroinitiator, 0.02 mol% of **10[Br]** and HMA monomer resulted in the formation of poly(methylmethacrylate)-co-poly(hexylmethacrylate) copolymer (PMMA-co-PHMA), with ^{1}H-NMR analysis showing the increase of the characteristic methylene bridge signal at *ca.* 4 ppm in $CDCl_3$ (Figure 9). If associated with the increase of M_n that is observed on going from the PMMA macroinitiator (M_n = 9800 g/mol) to the PMMA-co-PHMA copolymer (M_n = 16700 gmol) these results might suggest the possibility of exploiting the obtained living polymer as macroinitiator for preparing block copolymers.

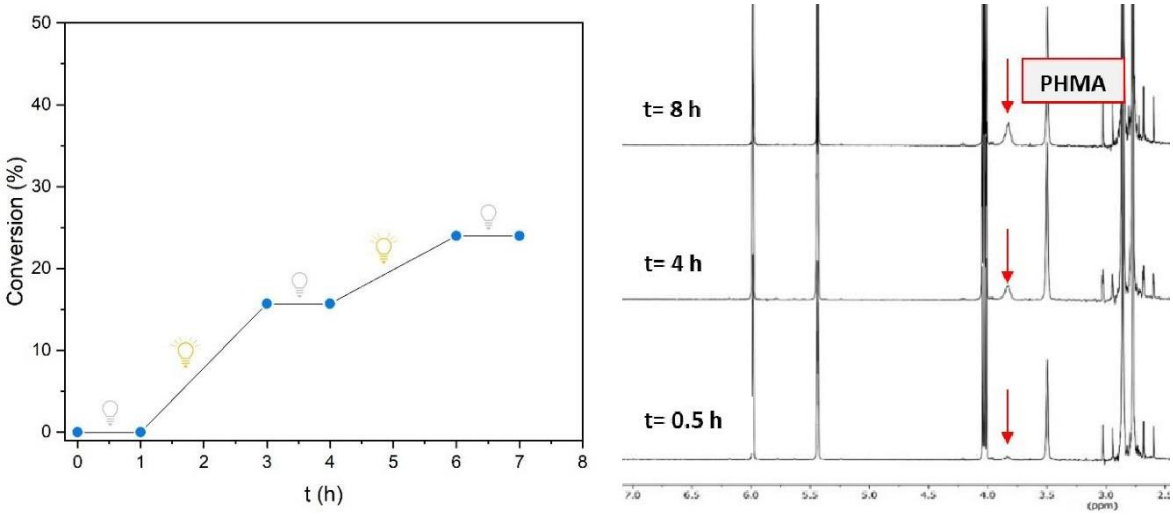

Figure 9: (sx) Polymerization of MMA with 0.02 mol% of **10[Br]** with two light-on periods; (dx) Overlayed ^{1}H-NMR (0.5, 4 and 8 hrs from the bottom up) of PMMA-co-PHMA copolymer obtained by reaction of PMMA-macroinitiator and 0.02 mol% of **10[Br]**, $CDCl_3$, 400 MHz

Importantly, model compound *fac*-[Ir(ppy)$_3$] was tested as well as photo-ATRP catalyst using our CFL lamps set up (entry 41, Table 3). It is worth noting how the polymerization profile obtained with *fac*-[Ir(ppy)$_3$] resemble the trend given by our complexes presented herein. A good control was achieved in the first 4 hours with linear relationship between $\ln(M_0/M)$ vs reaction time as well as between M_n vs χ. Then, a slight decrease in kinetic and M_n slope was observed, together with PDI values ranging from 1.3 to 1.7 (Figure 10). Therefore, a further development of the reaction set-up could be the key for the optimization of the photoactivated system, making our Ir(III) complexes promising alternatives to the homoleptic model.

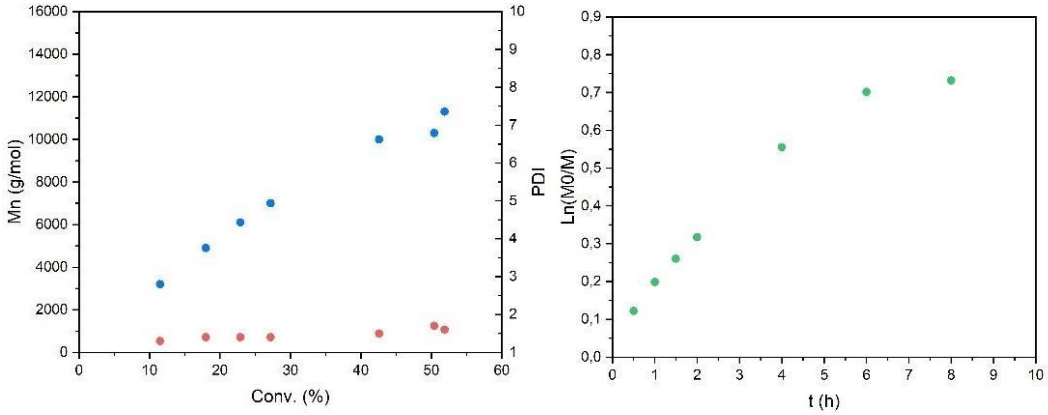

Figure 10. (sx) Polymerization profile of MMA, under argon, CFL set-up; (dx) Kinetic plot; Cat.: 12 (Ir(ppy)$_3$), [MMA]:[EBPA]:[Cat] = 1:0.004:0.01%

Transient Spectroscopy

Transient absorption spectroscopy (TAS) of three selected compounds was performed to gain more insights on the photochemical pathways triggering the photoinduced polymerization. Among the series, we have selected the standard *fac*-**[Ir(ppy)$_3$]**, the reference compound **1[Br]** and one of the best and worst performers, **10[Br]** and **5[Br]** respectively. The (ns-μs) TA spectra of these molecular Ir(III) photocatalysts upon 355 nm excitation in de-aerated DMF solution are reported in Figure 11. The 355 nm laser excitation led to the population of the lowest triplet charge transfer state within our instrumental response (FWHM = ca. 100 ns with 350 Ω impedance). Generally, spectra were recorded between 340 and *ca.* 450 nm according to the solvent transparency window (lowest wavelength) and the onset of the intense spontaneous emission, common to all the Ir(III) chromophores. Within this interval, all the complexes exhibited a bleach that mirrors the ground state absorption manifold around 400 nm. The sole exception is represented by **5[Br]**, whose triplet state is more absorbing than the ground state over the entire spectral range herein considered, and only a dip in the absorption band can be appreciated at *ca.* 410 nm (Figure 11 b). Intense absorption bands of the triplet state are observed in the 340– 380 nm and 420 - 500 nm interval, which leads to well defined isosbestic points for **1[Br]** and **10 [Br]** at *ca.* 380 and 420 nm. In contrast, TAS (Figure S129 a) of the reference compound *fac*-[**Ir(ppy)$_3$**] is dominated by bleached bands, which nicely mirror its ground state absorption. The excited state lifetime (τ_0) extracted from mono exponential fits of the ΔA decays, averaged over three different wavelengths around the bleaching minimum (as for **1[Br], 10 [Br]** and *fac*-**[Ir(ppy)$_3$]**) afforded values in agreement with the experimental emission studies discussed previously. In the case of **5[Br]**, the lifetime was extracted from the relaxation of the intense high energy absorption. τ_0 varies according to the series **5[Br]** (0.30 μs) < **10[Br]** (0.97 μs) < *fac*-**[Ir(ppy)$_3$]** (1.65 μs) < **1[Br]** (2.03 μs).

When a 40-fold excess of EBPA was added in the mixture as electron acceptor, we observed a change in the shape of the absorption spectra at short delays (0-13 μs, Figure 11 d-e-f and Figure S129 b) and different time evolution kinetics which are no longer mono exponential. This is particularly evident in the case of *fac*-**[Ir(ppy)$_3$], 1[Br]** and **10 [Br]** while **5[Br]** is largely unchanged. In deoxygenated solutions, *fac*-**[Ir(ppy)$_3$]**, **1[Br]** and **10[Br]**, evolve to a long lived state, which survives well into the ms time scale (Figure S129 and Figure 11, panels g,h,i), assigned to the Ir(IV) state generated upon oxidative quenching (electron transfer to EBPA) of the Ir(III) triplet state.

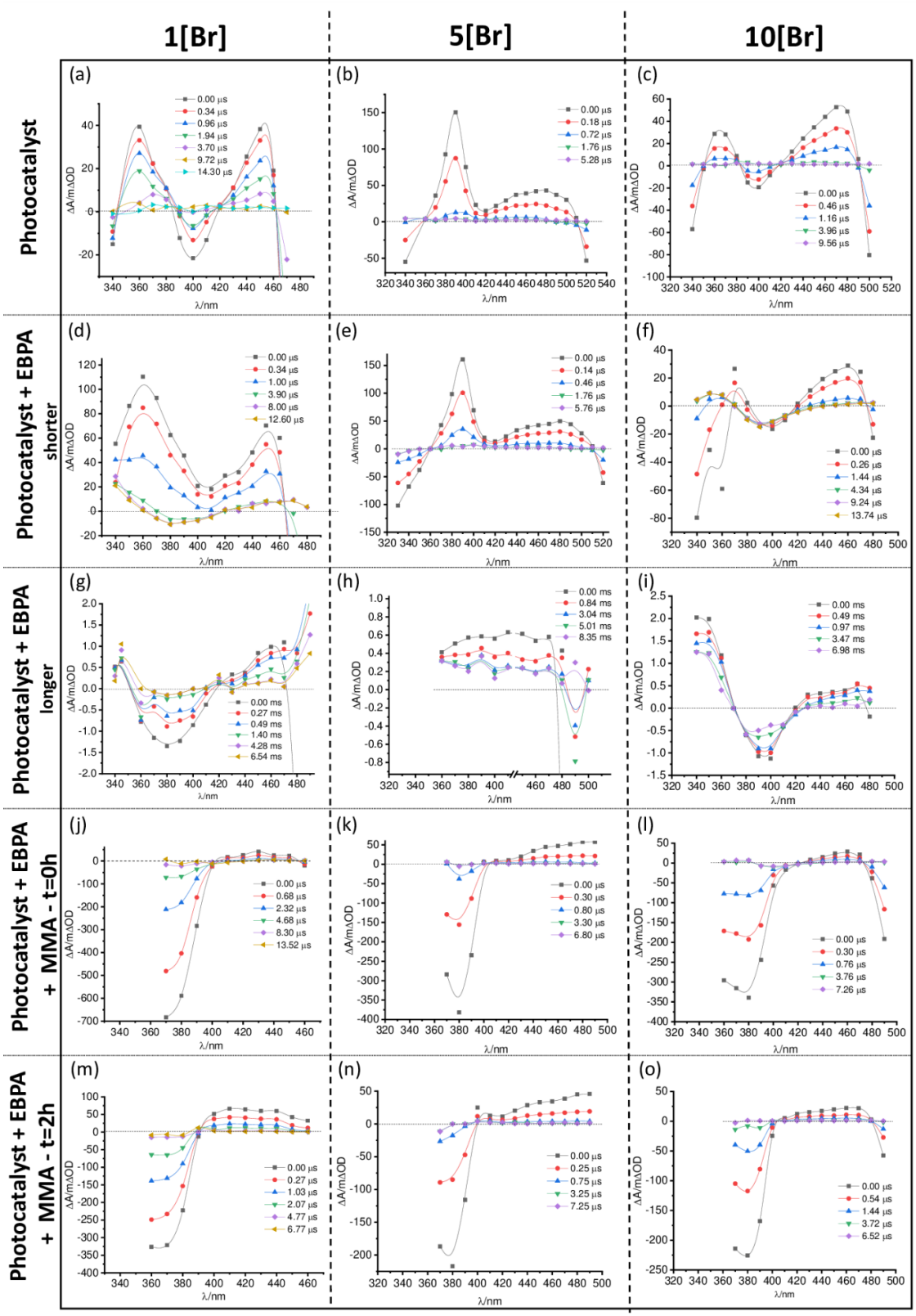

Figure 11: Transient absorption spectra for **1[Br]**, (c) **5[Br]** and (d) **10[Br]** for the different described situations in DMF solution. Laser Power: 9 mJ/cm^2/pulse

In the case of *fac*-**[Ir(ppy)$_3$]**, the evolution to the long-lived state occurs well within the FWHM of laser pulse (≤ 100 ns, λ = 380 nm). According to the kinetics at 400 nm, a fast process was observed

also for **10[Br]**. The analysis of the decay close to 420 nm, in proximity of one of the isosbestic points and where the excited state shows just a small residual positive absorption, displayed a bleach within the duration of the laser pulse when EBPA is present (Figure S131). TAS of **1[Br]** in presence of EBPA resulted in the removal of the excited state isosbestic points since 0 delay (corroborated by the transient spectrum at FWHM = 7 ns, Figure S130), in accordance with the absence of the bleaching band. Instead, intense absorption processes centered around 370 and 450 nm are present (Figure 11 d). This indicates that a new electronic state is achieved when **1[Br]** is photoexcited in the presence of an excess of EBPA. However, these absorption bands further decay with a lifetime of *ca.* 1 μs to a long-lived state, completely populated during the first 3 μs after the laser pulse. This is characterized by a broad bleaching band spanning in the 350-420 nm interval, with a minimum at 380 nm. After this final state is populated, no further spectral evolution can be observed into the millisecond time scale (Figure 11 g). Similar dynamics and spectral fingerprints are observed when $(NH_4)_2S_2O_8$ is used as electron acceptor (Figure S132), albeit with some differences in the relative intensity and shape of the absorption bands. We rationalized this behavior as the dissociation of (**1[Br]$^+$-Acceptor$^-$**) intermolecular ionic couple, where either EBPA or $S_2O_8^{2-}$ act as electron acceptors. Control measurements performed on **5[Br]** at longer time scales revealed only a minor presence of long lived Ir(IV) (ΔA ≈ 0.2 mΔOD), which is at the limit of the sensitivity of our spectrometer. This confirmed that the electron donation form **5[Br]**, characterized by the most positive E^*_{ox} within this series, is largely inefficient, corroborating the excited state oxidative quenching mechanism and the initiation step in the photo-ATRP. The photophysical behavior of the selected Ir(III) compounds was also observed in conditions relevant to the photopolymerization experiments, with [Ir]:[EBPA]:[MMA]=1:40:10000 molar ratios. At 355 nm, no relevant absorptions from MMA and EBPA were observed, thus excitation only involves the Ir(III) photocatalyst. In such conditions, we observed a change in the shape and relative intensity of the TAS of all the complexes. This was probably due to the nature of the solvent medium, which included a 10000-fold excess of MMA. For **1[Br]**, **10[Br]** and *fac*-[**Ir(ppy)$_3$**] an intense bleaching band between 360 and 400 nm (Figure 11 j, k, l and S129 c) that evolved within the laser pulse to a long-lived state was observed. Only weaker absorptions above 400 nm were detected. In the case of **5[Br]**, which is substantially inactive in promoting the oxidative quenching of the triplet state, transient decays were completed in 7 μs, indicating that the prominent bleaching observed for the complexes at early delays (0-2 μs) is indeed to the triplet state contribution. The Ir(IV) charge-separated state achieved in the presence of MMA is long lived, reaching within 4 μs a steady state with a permanent residual 450 nm

absorption. The population of such state is faster according to *fac*-[**Ir(ppy)$_3$**] (300 ns, comparable with the pulse width) > **10 [Br]** (≈ 400 ns) > **1 [Br]**. As observed previously, **1[Br]** evidently displays two kinetic components, having about the same amplitudes, a first one with a lifetime of 450 ns and much slower second one with a lifetime of the order of 1.7 µs, consistent with the behavior reported before. In all cases, the residual long lived amplitude at 450 nm is 25 to 30 % of the initial amplitude (Figure 12 a), with only a marginal evolution observed in the following µs. The photophysical experiments performed after 2 hours of polymerization, carried out with the same setup discussed in the previous section, (Figure 11 m, n, o and Figure S129 d) showed for all Ir(III) complexes spectral features similar to those just described. As the solvent medium is changing due to the formation of long polymer chains, some minor changes occur in the TAS, highlighting at early delays a decreased bleaching intensity compared to the longer wavelength absorption. Interestingly, after two hours polymerization, we observe a faster recovery of the long lived Ir(IV) state, with time constants of 2 to 5 µs, achieving a residual amplitude < 1/10 of the initial ΔA within the time window under consideration (Figure 12 b). This indicates that regeneration of Ir(III) probably occurs by reaction with the propagating polymer radicals. To the best of our knowledge, the increased concentration of $[Br]^-$ generated by EBPA dissociation can act as a Ir(IV) scavenger, seems to be ruled out based on the endo-ergonicity we infer from the cyclic voltammetry, where no bromide oxidation is observed before intercepting the Ir(III)/(IV) process DMF.

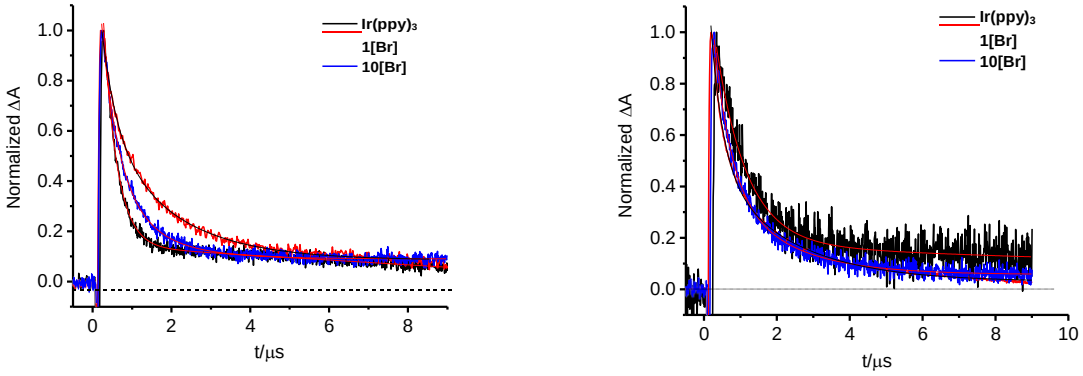

Figure 12: 450nm kinetics for **Ir(ppy)$_3$**, **1[Br]** and **10[Br]** in the presence of EBPA (40:1) and the MMA (10000:1) at (sx) 0h and (dx) 2h of polymerization

Conclusion

A new family of Ir(III) complexes with general formula [Ir(C^N)$_2$(N^N)][Br] was designed, synthesized and fully characterized. The compounds were tested as photocatalysts in the photoactivated ATRP

of MMA. After an extensive screening and study of the photophysical properties of each Ir(III) species, the key factors for this application were pointed out. All the complexes were capable of photoinitiating the polymerization of MMA, but a good control and, in general, the best performances were exhibited by the ionic Ir(III) complexes like **10[Br]** and **11[Br]**, in which of both the C^N and the N^N ligands were decorated with electron donor (ED) group in order to confer photophysical and redox properties similar to those of the *fac*-Ir(ppy)$_3$ catalyst model. Moreover, the nature of the counterion appeared to be essential for the accomplishment of the photo assisted process. In fact, by following a screening that encompassed various anions, bromide was selected as the best counterion for the cationic Ir(III) based photocatalysts. At the same time, the choice of light sources affected the catalytic performances it was of fundamental importance to select lamps whose emission spectrum could properly overlap with absorption spectra of the catalysts, together with ensuring adequate light intensity. Keeping in mind these considerations, we were able to reach encouraging results by implementing a "handcrafted" set up for preparing living polymers promoted by the irradiation with a "traditional" CFL source. The living nature of the polymer was proved by exploiting the latter as a macroinitiator in the preparation of block copolymers, confirming our new complexes as promising photocatalysts applicable to controlled/living radical polymerization (CRP) techniques. In addition, the outcomes obtained from the combination of transient absorption spectroscopy (TAS) experiments and DFT theoretical calculations performed on a selected series of our Ir compounds in comparison to the *fac*-[Ir(ppy)$_3$] model, allowed both to further confirm the role played by the Ir(III)-based species in the pathway to the photoassisted polymerizations, and to rationalize the factors - such as the displaying less positive E^*_{ox} and the concomitant faster population of the Ir(IV) charge-separated state formed in the presence of MMA - that were highlighted by the best performers among the whole series of the Ir(III) ionic complexes described herein.

Experimental Section

General considerations. Unless otherwise specified, reagents and solvents were obtained commercially (Merck, Alfa Aesar and Strem Chemicals) and used as received without any further purification. (N^N) and (C^N) ligands, $[Ir(C^N)\text{-}\mu\text{-}Cl]_2$ dimers and ATRP reactions were carried out under argon atmosphere following standard Schlenk protocols. The purification of (N^N) and (C^N) ligands was performed via column chromatography by using SiO_2 as stationary phase, while Ir(III) complexes required Al_2O_3. ESI-mass spectra were recorded using a Waters ZQ-4000 mass spectrometer (CH_3CN as the solvent). Nuclear magnetic resonance spectra (^1H and ^{13}C) were recorded using a Varian Mercury Plus 400 (^1H, 399.9; ^{13}C, 101.0 MHz). ^1H and ^{13}C chemical shifts were referenced to residual solvent resonances.

Photophysics. Absorption spectra were recorded at room temperature using an Agilent Cary 100 UV-vis spectrometer. Uncorrected steady-state emission and excitation spectra were recorded on an Edinburgh FLSP920 spectrometer equipped with a 450 W xenon arc lamp, double excitation and single emission monochromators, and a Peltier-cooled Hamamatsu R928P photomultiplier tube (185−850 nm). Emission and excitation spectra were acquired with a cut-off filter (395 nm) and corrected for source intensity (lamp and grating) and emission spectral response (detector and grating) by a calibration curve supplied with the instrument. The wavelengths for the emission and excitation spectra were determined using the absorption maxima of the MLCT transition bands (emission spectra) and at the maxima of the emission bands (excitation spectra). Quantum yields (Φ) were determined using the optically dilute method by Crosby and Demas[28] at excitation wavelength obtained from absorption spectra on a wavelength scale (nm) and compared to the reference emitter ($[Ru(bpy)_3]^{2+}$in H_2O) by the following equation:[29]

$$\phi_s = \phi_r \left[\frac{A_r(\lambda_r)}{A_s(\lambda_s)}\right]\left[\frac{I_r(\lambda_r)}{I_s(\lambda_s)}\right]\left[\frac{n_s^2}{n_r^2}\right]\left[\frac{D_s}{D_r}\right]$$

Where A is the absorbance at the excitation wavelength (λ), I is the intensity of the excitation light at the excitation wavelength (λ), n is the refractive index of the solvent, D is the integrated intensity of the luminescence, and Φ is the quantum yield. The subscripts r and s refer to the reference and the sample, respectively. A stock solution with an absorbance > 0.1 was prepared, then a 10 times diluted solution was obtained, resulting in absorbance of about 0.07/0.08 depending on the sample considered. The Lambert-Beer law was assumed to remain linear at the concentrations of the solutions. The degassed measurements were obtained after the solutions were bubbled for 10

minutes under Ar atmosphere, using a septa-sealed quartz cell. Air-equilibrated $[Ru(bpy)_3]Cl_2/H_2O$ solution ($\Phi = 0.028$)[30] was used as reference. The quantum yield determinations were performed at identical excitation wavelengths for the sample and the reference, therefore deleting the $I(\lambda r)/I(\lambda s)$ term in the equation. Emission lifetimes (τ) were determined with the single photon counting technique (TCSPC) with the same Edinburgh FLSP920 spectrometer using pulsed picosecond LED (EPLED 365, FWHM < 800ps) as the excitation source, with repetition rates between 1 kHz and 1 MHz, and the above-mentioned R928P PMT as detector. The goodness of fit was assessed by minimizing the reduced $\chi 2$ function and by visual inspection of the weighted residuals. To record the 77 K luminescence spectra, the samples were put in a quartz tube (2 mm diameter) and inserted in a special quartz Dewar filled with liquid nitrogen. The solvent used in the preparation of the solutions for the photophysical investigations was of HPLC grade. Experimental uncertainties are estimated to be ±8% for lifetime determinations, ±20% for quantum yields, and ±2 nm and ±5 nm for absorption and emission peaks, respectively.

Stern Volmer quenching experiments. 2 mL of 1.04 to $1.22*10^{-4}$ M anhydrous and degassed DMF solutions of the Ir(III) complexes were placed in a septa-sealed quartz cuvette. Successive aliquots of EBPA (9x5 µL) were added with a micropipette; emission spectra were recorded after each addition, while lifetimes were acquired in absence (τ_0) or at the end of the emission titration experiments (τ).

Cyclic Voltammetry. $TBAPF_6$ (tetrabutylammonium hexafluorophosphate, Merck) was used as received as the supporting electrolyte; anhydrous DMF (99.8%, Sigma Aldrich) was used as received and thoroughly degassed under N_2 before each measurement. Electrochemical experiments were recorded with a Metrohm Autolab PGSTAT302N potentiostat-galvanostat using a Calomel electrode as reference (303/SCG/6 – Amel Electrochemistry) and a Platinum solid electrode (492/Pt/2 – Amel Electrochemistry) as working electrode.

X-Ray Crystallography. Crystal data and collection details for **[1][BF_4]·solv** and **[2][PF_6]·CH_2Cl_2** are reported in Supporting Information, Table S4. Data were recorded on a Bruker APEX II diffractometer equipped with a PHOTON2 detector using Mo–Kα radiation. The structures were solved by direct methods and refined by full-matrix least-squares based on all data using F2.[31] Hydrogen atoms were fixed at calculated positions and refined using a riding model. The unit cell of **[1][BF_4]·solv** contains an additional total potential solvent accessible void of 529 $Å^3$ (*ca*. 14% of the cell volume), which is likely to be occupied by highly disordered solvent molecules. These voids have been treated using the SQUEEZE routine of PLATON.[32] Deposition Number(s) <url

href="https://www.ccdc.cam.ac.uk/services/structures?id=doi:10.1002/chem.202400393">
2328594 (for **[1][BF_4]·solv**), 2328595 (for **[2][PF_6]·CH_2Cl_2**) </url> contain(s) the supplementary crystallographic data for this paper. These data are provided free of charge by the joint Cambridge Crystallographic Data Centre and Fachinformationszentrum Karlsruhe <url href="http://www.ccdc.cam.ac.uk/structures">Access Structures service</url>.

Light sources. The intensity of the Led strip used as light source was measured with a power meter within 5 cm of the crystallization dish used as the support. The resulting surface power density is 3 mW/cm^2. CFL households lamp (2X12W, E27, 6500K, Osram) were used as light source. A fan was placed above each photoreactor to maintain the temperature below 30°C.

Gel Permeation Chromatography (GPC). The average molecular weights and polidispersity index values were determined using HPLC Lab Flow 2000 apparatus with injector Rheodyne 7725i, refractive index detector Knauer RI K-2301 and column TSKgel GMH$_{HR}$-N, 5 µm, 7.8x300 mm in DMF.

Transient Absorption Spectroscopy. Transient absorption spectroscopy in the ns-ms time scale was performed with a previously described time resolved apparatus.[33] The samples were excited by 355 nm harmonic of a Nd:YAG laser (continuum Surelite II) by defocusing the laser beam. The monochromatic light probe beam was generated by a 150 W Xe lamp coupled with an Applied Photophysics monochromator and was pulsed for time windows lower than 400 µs to increase the signal-to-noise ratio (S/N). To further act on the S/N ratio, multiple shots were acquired, and the signal was pre-amplified with different impedances (varying between 350 Ω to 1 M Ω) depending on the selected time windows. The Samples were either composed by deoxygenated DMF or CH_3CN solutions of the 6.77x10^{-5} mM iridium catalyst, first alone and then in the presence of a 40-fold excess of EBPA initiator (40:1). Measurements were also carried out during the polymerization, by introducing EBPA (40:1) and MMA (10000:1). To validate the oxidative quenching pathway, transient absorption analysis was also conducted in the presence of $S_2O_4^{2-}$ anion (1:240) as electron acceptor.

Quantum chemical computations. The geometry optimization of the dye structures was performed with Gaussian 09 A2.[34] First equilibrium geometries were computed in vacuo (restricted B3LYP-LANL2DZ) and the geometry output and wavefunction from such calculation were used to refine the ground state geometry at the DFT-B3LYP/LANL2DZ level[35] (in the presence of CH_3CN described as a polarizable dielectric continuum model (Integral Equation Formalism Continuum Polarization Model, IEFCPM). TD-DFT spectra were computed in ACN at the B3LYP-CEP121G/IEFPCM[36] by considering the first 40 lowest energy vertical excitations and using the guess wavefunction

generated from the LANL2DZ/ACN calculation. Experimental Spectra in CH_3CN and DMF were fully comparable, and the electronic properties extracted from the ACN computation can be safely extended to DMF (Figure S90). Kohn Sham (KS) molecular orbitals were visualized as isodensity (isovalue 0.001) surfaces with Gaussview 5. Wavefunction analysis and EDDM of the optical transitions were obtained with Multiwfn 3.3.9.[37]

Conflicts of interests

The Authors have no conflicts to declare.

Acknowledgements

The authors wish to thank the Toso Montanari Foundation for financial support. This publication is part of the project PNRR – NGEU, which has received funding from the MUR – DM352/2022.

Table of Contents

Graphycs

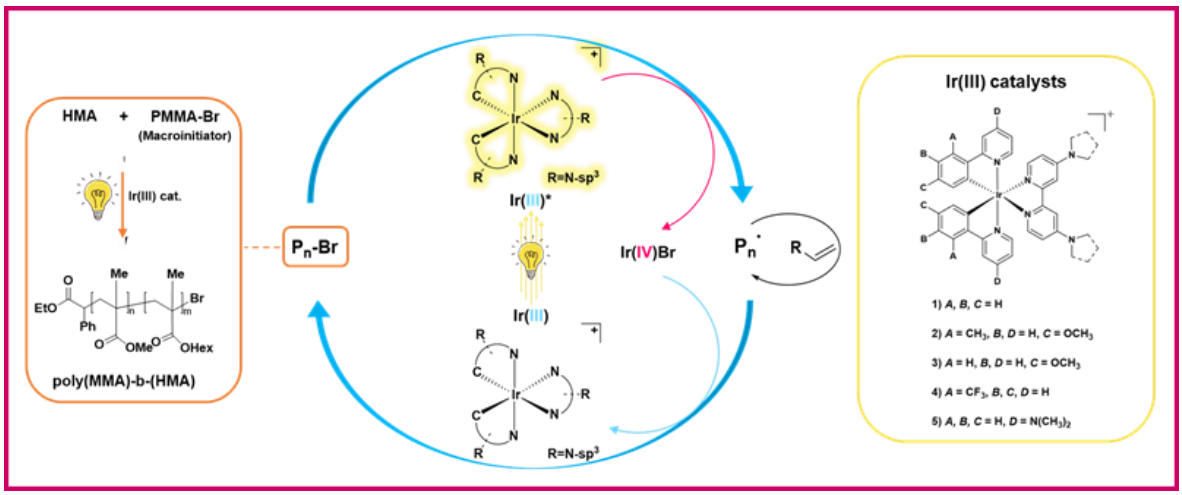

Text:

A new family of ionic Ir(III)-complexes was designed, prepared and assessed for the visible light assisted ATRP of methyl methacrylate (MMA). A complete experimental and mechanistic study is performed to shed light on the factors responsible for a proper control of the polymerization process.

References

[1] D. A. Nicewicz, D.W.C. MacMillan, *Science* **2008**, *322*, 77 – 80.

[2] M. A. Ischay, M. E. Anzovino, J. Du, T. P. Yoon *J. Am. Chem. Soc*. **2008**, *130*, 12886 – 12887.

[3] J. M. R. Narayanam, J. W. Tucker, C. R. J. Stephenson *J. Am. Chem. Soc.* **2009**, *131*, 8756 – 8757.

[4] a) C. K. Prier, D. A. Rankic, D. W. C. MacMillan, *Chem. Rev.,* **2013**, *113*, 5322-5363; b) A. Y. Chan, I. B. Perry, N. B. Bissonnette, B. F. Buksh, G. A. Edwards, L. I. Frye, O. L. Garry, M. N. Lavagnino, B. X. Li, Y. Liang, E. Mao, A. Millet, J. V. Oakley, N. L. Reed, H. A. Sakai, C. P. Seath, D. W. C. MacMillan *Chem. Rev.* **2022**, *122*, 1485−1542; c) K. Pak Shing Cheung, S. Sarkar, V. Gevorgyan *Chem. Rev.* **2022**, *122*, 1543−1625

[5] a) M. Chen, M. Zhong, J. A. Johnson *Chem. Rev.* **2016**, *116*, 10167–10211; b) V. Ferraro, C. R. Adam, A. Vranic, S. Bräse *Adv. Funct. Mater.* **2023**, 2302157.

[6] a) S. Dadashi-Silab, S. Doran, Y. Yagci *Chem. Rev.* **2016**, *116*, 10212–10275; b) X. Pan, M. A. Tasdelen, J. Laun, T. Junkers, Y. Yagci, K. Matyjaszewski *Prog. Polym. Sci.* **2016**, *62*, 73–125.

[7] a) B. P. Fors, C. J. Hawker, *Angew. Chem. Int. Ed.*, **2012**, *51*, 8850 –8853; b) N. J. Treat, B. P. Fors, J. W. Kramer, M. Christianson, C. -Y. Chiu, J. Read de Alaniz, C. J. Hawker, *ACS Macro Lett*.,**2014**, *3*, 580−584.

[8] T. Hofbeck, H. Yersin *Inorg. Chem.* **2010**, *49*, 9290–9299

[9] a) A. B. Tamayo, B. D. Alleyne, P. I. Djurovich, S. Lamansky, I. Tsyba, N. N. Ho, R. Bau, M. E. Thompson *J. Am. Chem. Soc.* **2003**, *125*, 7377–7387; b) K. Dedeian, J. Shi, N. Shepherd, E. Forsythe, D. C. Morton *Inorg. Chem.* **2005**, *44*, 4445–4447; c) T. Sajoto, P. I. Djurovich, A. B. Tamayo, J. Oxgaard, W. A. Goddard, M. E. Thompson *J. Am. Chem. Soc.* **2009**, *131*, 9813–9822.

[10] P. -N. Lai, T. S. Teets *Chem. Eur. J.* **2019**, *25*, 6026 – 6037.

[11] a) J. Lalevée, M. Peter, F. Dumur, D. Gigmes, N. Blanchard, M.-A. Tehfe, F. Morlet-Savary, J. P. Fouassier *Chem. - Eur. J.* **2011**, *17*, 15027–15031; b) M.-A. Tehfe, M. Lepeltier, F. Dumur, D. Gigmes, J.-P. Fouassier, J. Lalevée *Macromol. Chem. Phys.* **2017**, *218*, 1700192; c) S. Telitel, F. Dumur, S. Telitel, O. Soppera, M. Lepeltier, Y. Guillaneuf, J. Poly, F. Morlet-Savary, P. Fioux, J.-P. Fouassier, D. Gigmes, J. Lalevée *Polym. Chem.* **2015**, *6*, 613–624.

[12] a) K. Matyjaszewski, *Macromolecules*, **2012**, *45*, 4015-4039; b) A. H. E. Müeller, K. Matyjaszewski, "*Controlled and Living Polymerizations: From Mechanisms to Applications*" Wiley-VCH Verlag GmbH & Co. KGaA, **2009**: K. Matyjaszewski, Chapter 3: "Radical Polymerization"; see also, c) J. Beaudelot, S. Oger, S. Peruško, T.-A. Phan, T. Teunens, C. Moucheron, G. Evano *Chem. Rev.* **2022**, *122*, 16365−16609.

[13] T. G. Ribelli, M. Fantin, J. -C. Daran, K. F. Augustine, R. Poli, K. Matyjaszewski, *J. Am. Chem. Soc.***2018**, *140*, 1525−1534.

[14] A. Pannwitz, A. Prescimone, O. S. Wenger, *Eur. J. Inorg. Chem*., **2017**, 609 – 615.

[15] N. Miyaura, A. Suzuki, *J. Chem. Soc., Chem. Commun.*, **1979**, 866-867.

[16] M. Nonoyama, *Bull. Chem. Soc. Jpn*., **1974**, *47*, 767.

[17] a)K. J. Suhr, L. D. Bastatas, Y. Shen, L. A. Mitchell, G. A. Frazier, D. W. Taylor, J. D. Slinker, B. J. Holliday *Dalton Trans.* **2016**, *45*, 17807-17823; D. Ma, Y. Qiu, L. Duan *Adv. Funct. Mater.* **2016**, *26*, 3438-3445;; M. Clemente-Leon, E. Coronado, C. J. Gomez-Garcia, A. Soriano-Portillo *Inorg. Chem.* **2006**, *45*, 5633.

[18] M.-J. Li CSD Private Communication, **2021**, CCDC 2073478

[19]J. Frey, B. F. E. Curchod, R. Scopelliti, I. Tavernelli, U. Rothlisberger, M. K. Nazaaruddin, E. Baranoff, *Dalton Trans.* **2014**, *43*, 5667

[20] [R. D. Costa, E. Orti, H. J. Bolink, S. Graber, S. Schaffner, M. Neuburger, C. E. Housecroft, E. C. Constable *Adv. Funct. Mater.* **2009**, *19*, 3456-3463.

[21] K. Nakamura, *Bull. Chem. Soc. Jpn*., **1982**, *55*, 2697–2705.

[22] L. Flamigni, A. Barbieri, C. Sabatini, B. Ventura, F. Barigelletti, *Top. Curr. Chem*., **2007**, *281*, 143–203.

[23] C. R. Bock, J. A. Connor, A. R. Gutierrez, T. J. Meyer, D. G. Whitten, B. P. Sullivan, J. K. Nagle *J. Am.Chem. Soc.* **1979**, 4815-4824.

[24] C. M. Cardona, W. Li, A. E. Kaifer, D. Stockdale, G. C. Bazan*, Adv. Mater.,* **2011**, *23*:2367–2371.

[25] F. De Angelis, S. Fantacci, N. Evans, C. Klein, S. M. Zakeeruddin, J.-E. Moser, K. Kalayanasundaram, H. J. Bolink, M. Grätzel, M. K. Nazeeruddin *Inorg. Chem*. **2007**, *46*, 5989-6001.

[26] X. Meng, R. Bai, X. Wang, F-F. Pan, L. He, *Dyes Pigm*., **2019**, *156*, 458-466.

[27] Z.J.Wu, B. Han, Z. W. Dai, P.C. Jin *Chem. Phys. Lett*. **2005**, *403*, 367-371

[28] G. A. Crosby and J. N. Demas, *J. Phys. Chem*., **1971**, *75*, 991-1024.

[29] D. F. Eaton, *Pure Appl. Chem*., **1988**, *60*, 1107-1114.

[30] K. Nakamura, *Bull. Chem. Soc. Jpn*., **1982**, *55*, 2697–2705.

[31] Sheldrick, G. M. Crystal structure refinement with SHELXL. Acta Crystallogr. C 2015, 71, 3-8.

[32] a) Spek, A. L. Single-crystal structure validation with the program *PLATON*. *J. Appl. Crystallogr.* **2003**, *36*, 7-13; b) Spek, A. L. Structure validation in chemical crystallography. *Acta. Crystallogr., Sect. D: Biol. Crystallogr.* **2009**, *D65*, 148-155.

[33] A. R. Marri, E. Marchini, V. Diez Cabanes, R. Argazzi, M. Pastore, S. Caramori, C. A. Bignozzi, P. C. Gros *Chem.Eur. J.* **2021**, *27*, 16260–16269.

[34] M. J. Frisch, G. W. Trucks, H. B. Schlegel, G. E. Scuseria, M. A. Robb, J. R. Cheeseman, G. Scalmani, V. Barone, B. Mennucci, G. A. Petersson, H. Nakatsuji, M. Caricato, X. Li, H. P. Hratchian, A. F. Izmaylov, J. Bloino, G. Zheng, J. L. Sonnenberg, M. Hada, M. Ehara, K. Toyota, R. Fukuda, J. Hasegawa, M. Ishida, T. Nakajima, Y. Honda, O. Kitao, H. Nakai, T. Vreven, J. A. Montgomery Jr., J. E. Peralta, F. Ogliaro, M. J. Bearpark, J. Heyd, E. N. Brothers, K. N. Kudin, V. N. Staroverov, R. Kobayashi, J. Normand, K. Raghavachari, A. P. Rendell, J. C. Burant, S. S. Iyengar, J. Tomasi, M. Cossi, N. Rega, N. J. Millam, M. Klene, J. E. Knox, J. B. Cross, V. Bakken, C. Adamo, J. Jaramillo, R. Gomperts, R. E. Stratmann, O. Yazyev, A. J. Austin, R. Cammi, C. Pomelli, J. W. Ochterski, R. L. Martin, K. Morokuma, V. G. Zakrzewski, G. A. Voth, P. Salvador, J. J. Dannenberg, S. Dapprich, A. D. Daniels, Ö. Farkas, J. B. Foresman, J. V. Ortiz, J. Cioslowski and D. J. Fox, Gaussian 09 Revison A.02.

[35] C. Latouche, D. Skouteris, F. Palazzetti, V. Barone *J. Chem. Theory Comput.* **2015**, *11*, 3281−3289

[36] G.R. Morello *J. Mol. Model.* **2017**, *23*, 174.

[37] T. Lu, F. Chen, *J. Comput. Chem.* **2012**, *33*, 580–592